Published in final edited form as:
Chem Mater. 2012 August 14; 24(15): 2952–2964. doi:10.1021/cm301148d.

Composition-structure relationships in the Li-ion battery electrode material $LiNi_{0.5}Mn_{1.5}O_4$

Jordi Cabana[1,*], **Montserrat Casas-Cabanas**[2,3], **Fredrick O. Omenya**[4], **Natasha A. Chernova**[4], **Dongli Zeng**[5,6], **M. Stanley Whittingham**[4], and **Clare P. Grey**[5,7]

[1]Environmental Energy Technologies Division, Lawrence Berkeley National Laboratory, Berkeley, CA 94720.

[2]Laboratoire CRISMAT, UMR CNRS ENSICAEN 6508, 14050 Caen, Cedex 4, France

[3]CIC Energigune, Parque Tecnológico de Álava. Albert Einstein 48, 01510 Miñano (Álava) Spain

[4]Department of Chemistry and Materials Science and Engineering Program, State University of New York at Binghamton, Binghamton, NY, 13902-6000, USA.

[5]Department of Chemistry, State University of New York at Stony Brook, Stony Brook, NY 11794-3400, USA

[6]Brookhaven National Laboratory, Upton, New York 11973

[7]Chemistry Department, Cambridge University, Cambridge, CB2 1EW, UK

Abstract

A study of the correlations between the stoichiometry, secondary phases and transition metal ordering of $LiNi_{0.5}Mn_{1.5}O_4$ was undertaken by characterizing samples synthesized at different temperatures. Insight into the composition of the samples was obtained by electron microscopy, neutron diffraction and X-ray absorption spectroscopy. In turn, analysis of cationic ordering was performed by combining neutron diffraction with Li MAS NMR spectroscopy. Under the conditions chosen for the synthesis, all samples systematically showed an excess of Mn, which was compensated by the formation of a secondary rock salt phase and not via the creation of oxygen vacancies. Local deviations from the ideal 3:1 Mn:Ni ordering were found, even for samples that show the superlattice ordering by diffraction, with different disordered schemes also being possible. The magnetic behavior of the samples was correlated with the deviations from this ideal ordering arrangement. The in-depth crystal-chemical knowledge generated was employed to evaluate the influence of these parameters on the electrochemical behavior of the materials.

[*]corresponding author: jcabana@lbl.gov.

Supporting Information Available: Deconvolution of the ^{6}Li MAS NMR spectrum of OH500C and derivative plots of the first cycle of lithium metal half cells. This material is available free of charge via the Internet at http://pubs.acs.org.

Keywords

Crystal-chemistry; lithium nickel manganese oxide; spinel; Li-ion batteries

Introduction

Lithium-ion batteries are the power source of choice in electric drive vehicles available in the market,[1] and are being considered for a number of stationary storage applications.[2] However mature as the technology may seem, improvements in terms of safety, life and, particularly, energy density are still required to fulfill the demand of these applications.[3] One strategy to increase the amount of energy that can be stored in a battery is to raise the voltage at the positive electrode, since the negative electrode materials already operate close to the potential of metallic lithium. $LiNi_{0.5}Mn_{1.5}O_4$ [4, 5] has emerged as a promising candidate because the potential (~4.7 V *vs.* Li^+/Li^0) at which lithium is removed from the structure is the highest among the viable options.[6] Recent studies have shown the promise of Li-ion batteries based on this material.[7–9] The most important barrier to applicability of $LiNi_{1/2}Mn_{3/2}O_4$ is precisely due to the high voltage of operation, which is outside the window of stability of the electrolyte solutions used in Li-ion batteries.[6] As a result, spurious reactions occur during cycling[10–13] that lead to passivation layers on the surface of the electrode which compromise the life of the whole device. This undesirable process is aggravated at small particle sizes due to the increase in surface area.[10, 14] Therefore, the conventional approach to increase the performance of an electrode through a reduction of diffusion lengths with nanostructured active materials[15–17] is precluded for $LiNi_{0.5}Mn_{1.5}O_4$, and, instead, large particles that have optimized transport properties are required. Consequently, full understanding of the bottlenecks to such transport in the bulk needs to be achieved. This correlation cannot be established without in-depth knowledge of the crystal chemistry (composition, structure) of the compound, as it critically affects the mobility of charge carriers in the material.[18, 19]

$LiNi_{0.5}Mn_{1.5}O_4$ crystallizes in a spinel structure with Li^+ ions located on the tetrahedral sites and the transition metal ions on the octahedral sites in an oxygen cubic close packed network. This structure favors fast 3-D lithium diffusion within the framework. The stoichiometric material has Ni and Mn in the +2 and +4 redox states, respectively,[5, 20] Li extraction formally occuring *via* the oxidation of Ni^{2+} to Ni^{4+}, the Mn^{4+} ions remaining as spectators. The distribution of cations on the octahedral sites is found to depend on synthesis conditions. Ni and Mn have been proposed to either order in the 4a and *12d* sites of a $P4_332$ space group or be randomly distributed in the 16d sites of a Fd-3m-type unit cell. An order-to-disorder transition has been reported by several authors to occur at around 700 °C.[21–23] The transition is associated both with a loss of oxygen in the sample[23, 24] and the generation of Mn^{3+} in the spinel structure, which is identified by the onset of electrochemical activity of the material around 4.0 V vs. Li^+/Li.[0.5] It has been proposed by some authors that these parameters are correlated, with oxygen loss creating anionic vacancies in the spinel lattice that, together with the presence of Mn^{3+}, induce structural disorder.[23, 25] However, direct evidence for oxygen vacancies is difficult to obtain because of the limited tools available to measure with high accuracy the content of O^{2-} in a solid. Although thermogravimetric analysis under several atmospheres is consistent with uptake and release of O_2,[23, 24] this phenomenon could be simply due to the formation of a rock salt secondary phase,[26] which has a lower oxygen-to-metal ratio. Some evidence of oxygen vacancies was provided using refinements of neutron diffraction data,[24] but other samples in the same study were found to contain Mn^{3+} with full occupancy of the oxygen site, suggesting that oxygen loss and manganese reduction are not correlated.

It has previously been shown that the structural characteristics of different $LiNi_{0.5}Mn_{1.5}O_4$ samples have an impact on both the mechanism of Li extraction[19, 21, 23] and their electrochemical performance; the disordered samples are generally considered to have better rate capabilities.[23] The origin of this improved performance is not fully understood. Indeed, first principle calculations indicate that the barriers for lithium motion are similar in both types of structure.[27] The elucidation of the structure-composition-properties relationship is further complicated by the fact that a complete picture of the interplay between the different ordering schemes, mechanism of oxygen loss and the formation of Mn^{3+} in the spinel structure, which creates carriers that could enhance electronic conductivity,[28, 29] remains to be fully revealed. In order to achieve this knowledge, simultaneous analysis of the sample by tools sensitive to multiple parameters and scales is required.

The aim of this work is to investigate the local and long-range structure so as to help identify the parameters that are critical for optimal electrochemical properties. With this aim in mind, we synthesized a series of samples formulated as $LiNi_{0.5}Mn_{1.5}O_4$ at different temperatures, using the same precursors and following similar synthetic approaches to those used by many studies in the literature.[24, 30–33] Such approach delivered a series of very different samples with which to explore the crystal-chemical space around this composition. Analysis of the possible cation arrangements was performed by combining neutron diffraction (ND), which provides long-range information that is sensitive to ions with similar atomic numbers (such as Ni and Mn), with Li magic angle spinning (MAS) nuclear magnetic resonance (NMR), a tool with sensitivity to very short length scales (1 to 2 chemical bonds). The composition of the samples was analyzed by ND, electron microscopy and X-ray absorption spectroscopy (XAS). Further insight into transition metal ordering and the presence of impurities was provided by the magnetic properties of the samples. The complete crystal-chemical picture that emerged from this combination of probes was employed to evaluate the influence of these parameters on the electrochemical behavior of the materials. This study complements our recently published analysis of the effect of microstructure on an extended series of samples.[14] The reader is referred to this earlier report for a complete characterization of particle size and morphology of the samples.

Experimental

Synthesis

Samples with initial nominal Mn/Ni and Li/transition metal (TM) ratio of 1/3 and 1/2, respectively, were synthesized from hydroxide precursors at different temperatures. A mixed nickel manganese hydroxide was prepared by the dropwise addition of 50 ml of a water solution containing stoichiometric amounts of $NiSO_4 \cdot 6H_2O$ and $MnSO_4 \cdot H_2O$ to 400 ml of a solution containing NaOH in a three-fold excess. The resulting brown powder was filtered, washed with water repeated times, heat-treated at 150°C overnight, and, finally, mixed with stoichiometric amounts of $LiOH \cdot H_2O$. The mixture was pelletized and fired in air at different temperatures ranging from 500 to 1000°C for 12 h. The cooling rate was set at 5°C/min for all samples. The sample made at 1000°C was subject to a second heat-treatment at the same temperature for 24 h. The samples are labeled OH“T”C, where “T” indicates the heat treatment temperature.

Crystal-chemical characterization

Powder ND data were obtained using the D1A high-resolution powder diffractometer at the Institut Laue Langevin (ILL). Data were taken at room temperature (RT) using a short wavelength of $\lambda = 1.39$ Å in order to assure a high accuracy for the determination of site occupations, with a step size of 0.1° on a 2θ domain ranging from 5° to 155°. All Rietveld refinements were carried out with the FullProf program[34] (Windows version, May 2010)

using the pseudo-Voigt profile function of Thompson, Cox and Hastings.[35] The electron diffraction (ED) patterns and TEM images were recorded with a JEOL 2010 electron microscope equipped with an EDS (energy dispersive spectroscopy) analyzer.

X-ray absorption near edge spectroscopy (XANES) at the Mn and Ni K-edges was collected in transmission mode on beamline 4-1 at the Stanford Synchrotron Radiation Lightsource (SSRL) at SLAC National Accelerator Laboratory (Menlo Park, USA). Samples were prepared in the form of finely ground powder smeared onto pieces of adhesive tape. Higher harmonics in the X-ray beam were minimized by detuning the Si(220) monochromator by 50% at the Mn edge and by 35% at the Ni edge. Energy calibration was carried out by using the first inflection points in the spectra of Mn and Ni metal foil as references, at 6539 and 8333 eV, respectively. Data for MnO was collected at BM29 beam line at ESRF (Grenoble, France) in an earlier study.[36] Experimental details can be found in the corresponding reference.

The ^{6}Li MAS NMR experiments were performed at 29.39 MHz on a Chemagnetics CMX-200 spectrometer (B_0=4.7 T) using a double-resonance 1.8 mm probe, with silicon nitride rotors spun at a speed of 38 kHz. All of the spectra were acquired following a rotor-synchronized Hahn echo sequence (90°-τ–180°-τ acquisition) and referenced to a standard 1 M ^{6}LiCl solution at 0 ppm. π/2 pulses of 3.5 μs were used, with an acquisition delay time of 0.2 s. Spectral deconvolution was performed using the NUTS NMR data processing software.

Measurement of magnetic properties

Magnetic properties were studied on Quantum Design MPMS and PPMS instruments. A SQUID magnetometer (Quantum Design MPMS XL-5) was used to measure dc magnetic susceptibility (χ=M/H, M is magnetization, H is applied magnetic field) of the samples from 400 to 2 K in a magnetic field of 1000 Oe. Field-cooled (FC) and zero-field-cooled (ZFC) magnetizations were measured over the same temperature range in the magnetic fields of 10 Oe. FC susceptibility was measured by cooling the sample in the magnetic field. Before taking ZFC data, the remnant magnetic field was quenched to less than 3 mOe, the sample was cooled to 2 K, then the magnetic field was applied and the temperature dependence was measured while heating the sample. Magnetization curves were measured at 2 K in the magnetic fields up to 9 T using Quantum Design PPMS. The sample was zero-field cooled to 2 K before the magnetization data was taken.

Electrochemical characterization

Electrochemical characterization was performed in a lithium metal half-cell configuration. For this purpose, composite electrode films were made by mixing the different $LiNi_{0.5}Mn_{1.5}O_4$ samples with acetylene black and polyvinylidene difluoride (PVDF, Kureha Corp.) and making a slurry in N-methylpyrrolidone (NMP). The slurry was cast onto aluminum foil, dried at room temperature, followed by a treatment at 100°C in vacuum. The ratio of $LiNi_{0.5}Mn_{1.5}O_4$: carbon : PVDF was 80 : 10 : 10. The active material loadings in the electrodes were approximately 3.5 mg/cm^2. Testing was performed using lithium metal as counterelectrode, Celgard 2400 as separator and 1 M $LiPF_6$ in ethylenecarbonate (EC) : dimethyl carbonate (DMC) in a 1 : 2 volume ratio as an electrolyte. The current density was set to a value corresponding to a C/10 rate, which corresponds to the delivery of the theoretical capacity (C=147 mAh/g) in 10 hours. The upper and lower cutoff voltages were set at 5.0 and 3.5 V, respectively.

Results and Discussion

Neutron Diffraction

ND patterns for all samples are shown in Figure 1. Among all the prepared samples, only sample OH700C exhibited superstructure peaks that can be indexed with a $P4_332$ space group, indicating the existence of Ni and Mn ordering. The diffraction pattern of the remaining samples could be indexed with the Fd-3m unit cell that corresponds to a disordered spinel. However, a modulation of the background scattering arising from short-range order was detected between 19° and 26°, 2θ, in most samples, being more marked in samples OH600C and OH800C. A shift of the main diffraction reflections of the spinel phase towards lower angles, consistent with an expansion of the unit cell, was also clearly visible for OH900C and OH1000C. Diffraction peaks corresponding to a secondary phase that could be indexed using a rock salt structure (space group Fm-3m) progressively appeared in the diffraction patterns of the samples made at 800°C and above. These reflections almost completely overlapped with those of the spinel phase in sample OH1000C. The presence of this rock salt phase has ubiquitously been reported in samples formulated so as to make a sample with composition $LiNi_{0.5}Mn_{1.5}O_4$.[37]

Rietveld refinement of sample OH700C was performed using the structure published by Gyffroy *et al.*,[38] with space group $P4_332$, as the starting point. Cell parameters, atomic parameters, profile parameters and background points were refined. Introduction of oxygen vacancies was attempted but the refinement always converged to a full oxygen occupation. The best fit (Figure 2a) was obtained when the occupancies of Ni and Mn were left to vary allowing the introduction of transition metal cation mixing. The refined composition can be written as $Li[Ni_{0.39}Mn_{0.11}]_{4b}[Mn_{1.42}Ni_{0.08}]_{12d}O_4$, which represents a slight excess of Mn content with respect to the theoretically formulated amount. Final atomic positions and Rietveld refinement details are summarized in Table 1 and atomic distances are detailed in Table 3. The final values compare well with previous literature reports.[17, 38]

The other members of the OH“T”C series were successfully refined with the Fd-3m space group, as expected from the absence of superstructure peaks (Table 2). However, two very small reflections at ~19 and 22°, 2θ (see asterisks in Figure 1) remained unindexed in samples OH800 and 900C. Attempts to account for them by introducing other obvious possible impurity phases such as Li_2MnO_3 or Li_2CO_3 into the Rietveld refinements did not yield satisfactory results. The refined profiles for samples OH500C and OH800C are shown as representative examples in Figure 2b and c. Variation from the nominal stoichiometry in the spinel phase was also investigated by refining oxygen occupancies but, as in sample OH700C, no oxygen deficiency was found. In contrast, manganese excess coupled with nickel deficiencies were found to be common to all the samples when the relative amounts of each cation were left to vary (but constrained to a full occupation of 16d sites). The obtained results suggest that the composition of the low temperature samples can be written as $LiNi_{0.45}Mn_{1.55}O_4$. This composition matched well, within error, the refined composition of sample OH700C (Figure 3). In contrast, above 800°C, the refined compositions of the spinel phase, $LiNi_{0.43}Mn_{1.57}O_4$ for sample OH900C and $LiNi_{0.33}Mn_{1.67}O_4$ for OH1000C, are indicative of a significant enrichment in manganese. These changes are consistent with the observed unit cell expansion, as the preservation of charge balance in the absence of oxygen vacancies is achieved by the replacement of Mn^{4+} by the larger Mn^{3+} ions (Figure 3).[39] Average TM-O and Li-O atomic distances were also found to gradually increase both for Mn/Ni and Li atoms (Table 3), as expected from this volume expansion.

Different compositions have been suggested for the secondary rock salt phase: $Li_{0.18}Ni_{0.82}O$ from the comparison of its lattice parameter with respect to those of NiO and MnO [5], or $(Li_{0.333}Mn_{0.5}Ni_{0.167})_xO$ if the same element ratio as the spinel is assumed, with x~0.93 at

900°C–950°C and x~1 at 1100°C.[24] Provided that no other impurities are present, the refined spinel compositions imply that the rock salt phase is nickel-rich (relative to the overall Ni:Mn ratio), in agreement with the first hypothesis, but not with the second. Attempts to evaluate its composition from the OH900C and OH1000C diffraction patterns were not successful due to the high correlation between scale factors, atomic positions and thermal parameters of both phases. Furthermore, for OH1000C, the reflections of both phases were found to strongly overlap. The secondary phase was ultimately added to the refinements in profile matching mode, which also precluded refinement of its fractional content. The cell parameter of this secondary phase is found to be close to 4.15 Å for all samples (Table 2) indicating that its composition varies little between samples. Hence, the Mn enrichment in the spinel phase is entirely driven by an increase in the rocksalt amount, which has a higher Ni:Mn ratio.

Electron Microscopy

In order to verify and complement the results from Rietveld refinements and obtain more insight into the rock salt phase, samples OH800C, OH900C and OH1000C were analyzed by electron diffraction (ED, Figure 4) and energy dispersive X-ray (EDX) analysis (Table 4). Of the ~30 individual crystallites that were examined in each sample, 11% correspond to this rock salt phase in sample OH800C, 22% in OH900C and 30% in OH1000C. These fractions should be regarded as approximate because they are obtained from a small population of crystals within the sample, and cannot be directly translated to quantitative phase fractions because of the different size of the observed crystallites. Nonetheless, they provide valuable insight into the change in the relative contributions of the different phases that confirms the trend of increasing in rocksalt secondary phase with temperature, with no additional impurities. Although the overall Mn:Ni ratio is found to be 3:1 in all samples, matching the theoretical ratios in the reactants, deviations from this ideal composition were found in the spinel phase as the synthesis temperature was increased. More specifically, the average Mn:Ni ratios of the crystallites with a spinel structure in samples OH800C, OH900C and OH1000C were 1.52:0.48, 1.56:0.44 and 1.70:0.30 for OH1000C. These values are in remarkably good agreement with the compositions obtained from Rietveld refinements of ND data and confirm the gradual increase of Mn content at the expense of Ni in the spinel phase. The Mn:Ni ratio was also determined for crystals of the rock salt phase that were well segregated from those of spinel phase. This ratio was found to vary slightly with synthesis temperature, ranging from 0.66:0.34 in samples OH800C and OH900C to 0.63:0.37 for sample OH1000C, in agreement with the lack of change in cell parameters, as discussed above. To the best of our knowledge, this is the first experimental evidence that the rock salt phase is in fact a manganese-rich oxide that contains both transition metals in a different cationic ratio than in the spinel phase, in contrast to previously proposed compositions.[5, 24] The general composition can be written as $(Li_xMn_{0.66}Ni_{0.34})_yO$ based on the general $M_{4a}O_{4b}$ formula for a disordered rock salt structure (Fm-3m space group), where the subindices indicate the corresponding Wyckoff sites. The values of x and y depend on whether this rock salt phase is cation deficient and on the manganese oxidation state.

Although in most cases the rock salt phase appeared as separate particles, examples were found of particles with discrete domains of the two structure types (Figure 4a). The inset shows the corresponding electron diffraction pattern, which is the result of overlapping the individual patterns of the two structure types. A dark-field image of the same particle formed from a (2, -2, 0) reflection that could be indexed to a rock salt-type structure is shown in Figure 4b. The insets show the individual zone axis of each crystallite (<111> zone axis for the rock salt and <101> zone axis for the spinel). The corresponding cell parameters of both phases were in agreement with those obtained from ND data. The formation of the rock salt phase on the surface of the spinel constitutes further proof of the spinel to rock salt

phase transformation within the same particle, as recently hypothesized for this system,[37] and is in agreement with a previous report in which the growth of an unidentified secondary phase was seen to form on the corner of a spinel particle.[21] Because both phases have the same cubic close packed oxide arrangement, the rock salt structure may be easily derived by cation migration and oxygen loss.[26] However, in this case the transition not only involves the displacement of lithium ions to octahedral sites as previously proposed in spinel systems[26] but also the migration of nickel ions towards the surface, where this rock salt phase forms. While the nickel content in the spinel phase gradually decreases, the rock salt domains, with a lower Mn:Ni ratio than the spinel, grow around the surface of the particles. The parent spinel phase is thus segregated into a composite that exhibits a spinel core and a rock salt surface structure. The fact that rock salt single-phase particles were abundantly observed by electron microscopy in our samples (not shown) suggests that either the transformation can come to completion within a particle or the rock salt domains detach before the transformation is complete. The fact that the two phases do not exhibit the same crystallographic orientation in Figure 4a might be due to the lattice mismatch between both phases at lower temperature, and would favor the second mechanism.

Nuclear Magnetic Resonance

Further insight into the local transition metal arrangement was obtained from the ^{6}Li MAS NMR spectra of these materials (Figure 5). The large observed NMR shifts are due to the existence of Li-X-M (where X=anion, M=transition metal) contacts, which lead to hyperfine interactions of the probe nucleus with the unpaired electrons in Ni and Mn.[40] Shifts at around 0 ppm are ascribed to interactions involving only diamagnetic ions. The fact that either very small or undetectable signals were observed in this region indicates that the samples are mostly free of impurities due to the unreacted lithium precursor. The most intense isotropic resonances from the spinel phase appeared between 500 and 1200 ppm. Because the rock salt secondary phase was proposed to contain Li, it should also contribute intensity to the spectra at around 700–800 ppm, particularly in the case for OH1000C, based on prior studies.[41]

The NMR spectra showed complex line shapes that changed noticeably with sample synthesis temperature. Because NMR is sensitive to all non-equivalent local environments for Li^{+} ions and to the presence of different transition metal ions,[42–45] the spectral complexity of the spinel samples was ascribed to the existence of a collection of environments with varying ratios of Ni and Mn in the first cation coordination shell. Most importantly, the presence of multiple resonances is an indication of crystallographic disorder in the sample. A fully ordered spinel sample with a Mn : Ni ratio corresponding to that of the overall spinel structure (1.5 : 0.5 in $LiNi_{0.5}Mn_{1.5}O_4$) would only contain the single lithium environment that is shown in the inset of Figure 6. A broad peak was observed for OH500C, with few distinct features, which evolved into a better-resolved spectrum, with more discrete peaks, for OH700C, and then broadened again at higher temperatures. This trend is consistent with the order-disorder transition that has been reported to occur at around 700°C, and is consistent with previous NMR data reported for this phase.[41, 46, 47] It is also in agreement with the appearance of diffuse scattering in the neutron diffractograms of OH600C and OH800C.

Below the order-disorder transition temperature, the ordering increased with the synthesis temperature, which is most likely a kinetic phenomenon that follows the increase in crystallinity of the samples observed in the powder diffraction patterns (Figure 1). In general, there was an apparent correlation between shift of the center of gravity in the series (Figure 5) and the extent of order. Three effects are proposed to come into play. First, and above 700°C, the content of Mn^{3+} increases (Figure 3), which results in a shift of the peaks to lower frequency.[41] Second, the increased linewidth and lower shift is due to the formation

of a significant fraction of rock salt, particularly at the highest temperature (1000°C). Below 700°C, the shift in center of gravity must be related to a different Ni/Mn ratio in the spinel phase, or different magnetic properties, assuming that the Mn oxidation state is similar.

Overall, the NMR results were in excellent *qualitative* agreement with the conclusions reached from the Rietveld refinement of ND data. More quantitative information about the ordering can however be obtained by combining these two techniques. Sample OH700C, which showed the simplest NMR spectrum, was chosen for the initial analysis. According to the Rietveld refinement results, this sample was formulated as $Li[Ni_{0.39}Mn_{0.11}]_{4b}[Mn_{1.42}Ni_{0.08}]_{12d}O_4$ with a $P4_332$ unit cell. The presence of Ni-Mn mixing is consistent with the appearance of more than one peak in the NMR spectrum. This spectrum was modeled using a number of assumptions. First, each Li has 12 TM cations (TM=Ni, Mn) in its first cation coordination shell (see inset in Figure 6), creating hyperfine interactions that dominate the NMR shifts. Random exchange between the two transition metal sites leads to new lithium environments with Mn : Ni ratios for the cations in the 1st coordination shell that deviate from the 3 : 1 value observed in the ideal ordered framework. The overall Mn : Ni ratio in each site (Table 1) was used as a constraint when calculating the different local environments. Because Ni^{2+}, Mn^{3+} and Mn^{4+} ions typically lead to very different hyperfine shifts in related oxide phases,[42–45] an approximation was made that the change in the Mn : Ni ratio and the Mn oxidation state were the major factors behind the spectral features. However, initially, only Ni^{2+} and Mn^{4+} ions were considered to simplify the analysis; the small amounts of Mn^{3+} found in ND data were assumed to have a smaller effect on the spectra and were initially ignored. The slight bond angle/distance deviations created by structural relaxations from the ideally ordered environments were also assumed to be small enough to only result in broadening of the corresponding peaks. For example, an environment with 1 Ni^{2+} substituted into the Mn^{4+} (*12d*) site and 1 Mn^{4+} into the Ni^{2+} (*4b*) site was considered to resonate at very similar shifts as one with no exchange, since both environments contain a total of 3 Ni and 9 Mn in the coordination shell in both cases.

The probabilities of finding a different number of Ni^{2+} or Mn^{4+} ions in the coordination sphere of lithium within this scenario were calculated for OH700C (Table 5). Environments with $P<0.01$ were considered to be virtually undetectable above the background of the spectrum. These values are roughly 2 orders of magnitude smaller than the highest probability values obtained in the calculation. Thus, only 5 different configurations, with from 1 to 5 Ni out 12 ions in the first cationic shell, were taken into account. In parallel, the ^6Li MAS NMR spectrum was deconvoluted with the minimum number of lines possible (Figure 6). A satisfactory fit was achieved with 5 peaks, at 788, 885, 952, 1020 and 1097 ppm. A signal with shifts close to 950 ppm was observed in a previous study on a sample with an even higher degree of structural order,[41] and, therefore, was assigned to the ideal ordered environment. Slight deviations in intensity between the fit and the experimental data were found around 950 ppm. These effects reflected the need for additional peaks in the deconvolution, implying that the real structure is more complex than a model with 5 environments due to the presence of some Mn^{3+} and additional local bond distortions. Nonetheless, the goodness of the fit warranted comparison of the intensity values with the probabilities of each environment in our model (Table 5). The values matched well within error, and could be ordered to correlate environments with larger amount of Ni^{2+} with higher hyperfine shifts. Further, this assignment paired the most intense resonance at 952 ppm with a general environment containing 3 Ni and 9 Mn ions, in agreement with the composition of the ideal ordered site. This model predicts that the absolute magnitude of shift induced by a Ni^{2+} cation is larger than that of a Mn^{4+} ion, which is in apparent contradiction with previous rules established from data on layered $LiMO_2$ (M=Ni, Co, Mn…),[45] albeit for different Li-O-M bond angles. The origin of this contradiction and, hence, the mechanism that could lead to higher shifts with higher number of Ni^{2+} ions in the

environment is not clear at this point. A theoretical and experimental study that assesses these effects and its role on resonance assignment will be the object of follow-up work. Interestingly, the resonance at 788 ppm was shifted by 100 ppm from the next highest frequency resonance, while the other resonances were separated by approximately 70 – 75 ppm. This environment is tentatively assigned to Li nearby more surrounding Mn^{3+} ions. This resonance corresponds to the Li environment nearby the most Mn ions, which is consistent with this assignment, since the Mn^{3+} ions (or more likely, an electron delocalized over more than one Mn^{4+}) will reside in Mn rich regions and rather than stoichiometric Ni/Mn ordered regions.

This approach was extended to model a disordered structure, where Ni and Mn are present on the same site and the only constraint is the Ni/Mn ratio in the overall compound. An average value of 0.45/1.55 was taken based on an average of the ND data. The results are found in Table 5. Environments with more than 6 Ni in the coordination shell were neglected because they showed $P<0.01$. Comparison with the results obtained for the partially ordered structure discussed above revealed that two more environments, corresponding to 0 and 6 Ni in the coordination shell, should be detectable as well. Other than these two environments, no environment has a noticeably higher probability of being present (Table 5). The NMR spectrum predicted by this model would show a larger degree of overlap because of local distortions caused by the reducing ordering, as is likely the situation in sample OH500C. A spectral deconvolution of this sample was attempted using these probabilities and peak shifts as soft constraints (Figure S1). The result was in qualitative agreement with the hypothesis, except for an unexplained higher intensity between 400 and 500 ppm, which we tentatively assigned to Mn^{3+}-rich regions. In the case of sample OH900C, the existence of distinct spectral features indicates that a spinel with partial short range ordering is present.

X-ray Absorption Near Edge Spectroscopy

An assessment of the electronic state of the transition metals in the spinel samples prepared in this study was carried out from Ni and Mn K edge XANES data. Virtually no change in the Ni K edge spectra was observed between samples OH500C and OH900C (Figure 7a and b), confirming that nickel is present as Ni^{2+}. Some of the spectral features at the edge were different for sample OH1000C. The most visible was the shift of the white line summit to slightly lower energies. A similar displacement at around 8370 eV and a decrease in relative intensity at the first inflection point of the edge were also observed. These new features are reminiscent of the signals resulting from Ni^{2+} in the rocksalt structure of NiO (Figure 7c). As a result, this spectrum could be described as a combination of signals from Ni in both types of cubic structures, consistent with the observation of significant amounts of $(Li_xMn_{0.66}Ni_{0.34})_yO$ rocksalt impurity at these synthesis temperatures.

Changes in the Mn K edge spectrum of OH1000C with respect to the other samples were observed as well. In this case a hard shift of the whole edge to lower energies was found, which was even more visible in the derivative plot (Figure 8), indicating increased presence of Mn^{3+} at 1000 °C. A slight shift to lower energy in the spectrum of OH900C with respect to OH500C–OH800C was also observed, consistent with both the increase in Mn^{3+} content in the spinel phase deduced from the stoichiometry obtained from ND data at temperatures above 800°C, and the shift of the ^6Li NMR spectrum of this sample to lower frequencies (see above). Mn K-edge spectra from the rock salt manganese (II) material MnO were very different, consistent with the higher oxidation state of the rocksalt phase found in these “spinel” samples. Since the rock salt accounted for a significant portion of the sample at high temperatures, (TEM and ND), it was concluded that Mn^{3+} predominates in its structure.

Magnetic characterization

The plots of the temperature dependence of the magnetic susceptibility (Figure 9) for the samples synthesized below 900°C revealed a ferrimagnetic ordering transition, accompanied by a strong susceptibility increase with temperature, consistent with previous reports on comparable samples.[48] The Néel temperature was the highest for OH700C, T_N = 126 K, and decreased to 116 – 118 K for OH600C and OH800C and to 109 K for OH500C. The higher Néel temperature for OH700C was ascribed to this sample containing the most ordered spinel phase.[48] OH900C and OH1000C showed broad susceptibility maxima centered around 35 K, a behavior more typical of a spin-glass or cluster-glass freezing than of ferrimagnetic ordering. The temperature dependences of the reciprocal susceptibility (inset in Figure 9) did not enter a linear regime in the temperature range studied for the samples synthesized below 1000°C because of the strong residual magnetic interactions, thereby precluding the fit of the data using the Curie-Weiss law in order to determine the effective magnetic moment.[27]

The comparison of field-cooled and zero-field cooled susceptibilities was used to further characterize the magnetic interactions as they are highly sensitive to magnetic ordering accompanied by net magnetic moment formation, and to spin-glass freezing. At such transitions the difference between FC and ZFC curves increases, making it possible to identify phases or clusters ordering at different temperatures. Figure 9b illustrates the low-temperature parts of the FC-ZFC curves, while Figure 9c magnifies the high-temperature region, where subtle deviations due to minority phases might occur. The FC and ZFC curves deviated at 122 K for OH700C, after a sharp ferrimagnetic transition, with no transitions observed at higher temperatures. However, the ZFC curve showed an additional maximum at 112 K, exactly where the ferrimagnetic transition for the disordered OH600C and OH800C samples occurs. This 112 K feature indicated a small degree of disorder in the spinel phase in OH700C, consistent with the ND and NMR results. The ZFC curves of OH900C and OH1000C revealed broad maxima typical of cluster-glass or spin-glass confirming the existence of significant structural disorder. While no high-temperature FC-ZFC deviations were found for OH600C, OH900C and OH1000C, both OH500C and OH800C showed pronounced irreversibility at temperatures as high as 350–400 K. It was hypothesized that these samples contain a small amount of ferrimagnetic impurities with a high ordering temperature. However, this impurity appeared to be different from the rock-salt phase in OH900C and OH1000C, which is either paramagnetic or antiferromagnetic.

The magnetization curve of OH700C (Figure 9d) indicated virtually no hysteresis and saturation at 3.12 μ_B per formula unit, consistent with ferrimagnetic ordering. This saturation magnetization decreased slightly to 3.10 μ_B for OH800C and OH600 C, and a slight linear increase at high fields was observed. Since some degree of local ordering was found in the samples by ND and NMR, the magnetic moments should also order locally in the same manner as in OH700C. Hence, the saturation magnetization values were similar. The minor linear increase of the magnetization came from disordered clusters, where the spins are likely frozen in a random configuration. The magnetization of OH500C, OH900C, and OH1000C did not saturate at the highest applied magnetic field of 9 T, achieving maximum values of 2.6, 2.0, and 0.8 μ_B, respectively. The lack of saturation was caused by both an increased structural disorder in the spinel phase, which destroyed the ferrimagnetic ordering, and the presence of the rock-salt phase.

No previous characterization of the magnetic properties of rock salt $Li_x(Ni_yMn_{1-y})_{1-x}O$ is available. Previous results for the $Ni_{1-y}Mn_yO$ solid solution shows that it contains a random distribution of Ni and Mn ions and is antiferromagnetic with a Néel temperature changing linearly between 118 K (MnO) and 523 K (NiO) with composition.[49] Earlier investigations of the $Li_xNi_{1-x}O$ series reported antiferromagnetic behavior for the phases $x \leq 0.3$, which

have a rock salt structure, and ferrimagnetism for phases with higher *x*, where an orthorhombic structure is present.[50] Cubic $Li_xMn_{1-x}O$ (x = 0.52) is paramagnetic at room temperature and undergoes a spin-glass transition at 42 K.[51] Thus, a disruption of antiferromagnetic order is expected upon substitution of Li into $Ni_{1-y}Mn_yO$. A similar effect should be observed in the spinel phase upon an increase in Mn content, as $LiMn_2O_4$ is a strongly frustrated antiferromagnet showing an onset of long-range order below 60 K with a significant portion of spins still disordered at lower temperatures.[52] These conclusions are consistent with the observation of broad ZFC maxima and a significant linear component in the magnetization curves for OH900C and OH1000C. This response suggests the existence of a broad range of magnetic clusters that order over a wide temperature range. It is also supportive of the presence of a significant Mn^{3+} content in the rock-salt phase in OH1000C, consistent with the XANES results, as the substitution of Li^+ and Mn^{3+} into NiO disrupts the antiferromagnetic order, and, thus, no antiferromagnetic transitions, as expected for $Ni_{1-y}Mn_yO$, are found.

Electrochemical characterization

The electrochemical properties of the materials were measured in order to evaluate the effect of the rich crystal-chemistry within the series. The voltage-capacity curve during the first cycle of the test cells is plotted in Figure 10. Only 40 mAh/g, equivalent to the extraction of less than 30% of the theoretical available lithium in $LiNi_{0.5}Mn_{1.5}O_4$, was obtained on charging OH1000C to 5.0 V. The poor performance indicates that the Ni, Mn-containing rock salt phase that forms a considerable fraction of the sample is electrochemically inactive. The TEM results above indicate that it can be found both as a coating of spinel particles and as segregated particles in this sample. Therefore, the existence of rock salt impurities not only lowers the overall capacity of the electrode, but also isolates the spinel domains from direct contact with the electrolyte. This secondary phase was found to be ubiquitous in the samples made in this study. Its minimization is necessary to optimize electrochemical properties.

Lithium extraction occurred mainly between 4.6 and 4.85 V in the samples made at T<1000°C, where oxidation of Ni^{2+} ions occurs.[20] A clear voltage plateau at 4.76 V was found in all samples, accompanied by another at 4.70 V that was most defined for OH800C and 900C (Figures 10 and S2). Several reports exist in the literature that indicate that the exact mechanism of lithium deintercalation is dependent on transition metal ordering.[19, 21, 22, 37, 53, 54] In turn, the mechanism of deintercalation is reflected macroscopically on the voltage profiles, particularly on the 4.70 V plateau. The subtle differences in shape found around this voltage are most likely a manifestation of the correspondingly subtle differences in transition metal ordering revealed in the previous sections. The existence of two plateaus separated by more than 50 mV is typically associated with a disordered structure. The gap is reported to shrink to 30 mV in samples labeled as “ordered”, and the two plateaus become virtually indistinguishable. However, the ND pattern of OH700C was indexed with a $P4_332$ superlattice due to a considerable degree of cationic ordering, as confirmed by MAS NMR, yet the gap between high voltage plateaus was 60 mV. It is concluded that an even closer to ideal Ni/Mn ordering is required for a smaller voltage gap to develop.

Electrochemical activity was also found below 4.4 V, which is commonly ascribed to the oxidation of Mn^{3+} in the spinel structure.[20] When the samples were made at 600°C≤T≤900°C, a shoulder centered at 4.1 V developed in the electrochemical profiles. The amount of capacity obtained during this process (Table 6) correlated well with the Mn^{3+} content in the spinel phase extracted from ND and EDS. A smooth increase in potential was observed at these potentials for OH500C (Figure 10), leading to an anomalously high capacity below 4.4 V (Table 6) compared to the refined composition. This sample shows the

largest ND reflections, indicating low crystallinity and/or small particle size. Indeed, as reported in a parallel study,[14] it comprised agglomerated secondary particles formed of primary particles of up to 50 nm in size. Smaller particle sizes imply an increase in the ratio of surface sites with respect to bulk, and a higher fraction of surface and sub-surface sites for lithium where the lattice is distorted with respect to a bulk crystalline sample. In combination with the low crystallinity, the result is a large range of local environments, as supported by the peak broadening in the ^{6}Li MAS NMR spectrum, and a range of potentials over which lithium can be extracted.[55] In turn, the capacity at low voltages for OH1000C is less than expected on the basis of the composition obtained from Rietveld refinements. Here, the large concentration of the rocksalt phase, which is largely inactive and partially coats the spinel phase, results in poor electrochemistry that is no longer quantitative for Mn^{3+} content.

The results obtained after completion of 30 charge-discharge cycles at C/10 are shown in Figure 11. Due to its very low initial capacity, data for OH1000C were excluded. A general improvement in initial specific capacity and cycle retention was observed with temperature of synthesis even at these fairly low rates. This improvement seems to be, at least partly, driven by the increase in crystallinity (Figure 1) and particle size.[14] The only exception was found in the capacity retention values of OH600C and OH700C, which were 87 and 84%, respectively (Table 6). These trends were largely amplified when the rate was increased.[14] The poor electrochemical performance of OH700C was attributed to its highest degree of Ni/Mn ordering, in agreement with earlier reports.[21, 29, 31, 56] Indeed, larger voltage polarization between charge and discharge was observed in this sample compared to OH600C, 800C and 900C (Figure 10). The increased polarization could be indicative of the detrimental effect of cationic ordering on transport properties. It is worth emphasizing the sensitivity of electrode performance to the extent of ordering. Even a structure like that of OH700C, where partial disorder of Ni and Mn occurs in a $P4_332$ superlattice, would not be desirable in order to optimize properties.

Conclusions

In-depth characterization of samples formally formulated as $LiNi_{0.5}Mn_{1.5}O_4$ has revealed the subtle crystal-chemical intricacies of this compound. Under the conditions chosen for the synthesis, the spinel samples systematically showed deviations from the theoretical stoichiometry, which involved an excess of Mn. The Mn excess resulted in the formation of some Mn^{3+} and was compensated (or driven) by the formation of a secondary phase with a rocksalt structure, not by the creation of oxygen vacancies. For the first time, it was reported that this rock salt phase contains both Mn and Ni in a lower ratio than in the spinel phase (*ca.* 2 to 1 *vs.* 3 to 1). Its formation occurs through the preferential extrusion of Ni out of the spinel particles, its content in the sample being correlated with the amount of Mn over-stoichiometry in the spinel phase. Detailed insight into the ordering schemes possible in "$LiNi_{0.5}Mn_{1.5}O_4$" was also provided. It was shown that samples showing superstructure reflections do not necessarily have perfect Ni and Mn ordering in a $P4_332$ superlattice. Local deviations from the ideal picture, as well as different disordered schemes, are possible. Indeed, some samples were shown to have some degree of preference for certain Ni/Mn distributions even if they crystallized in a disordered framework. The off-stoichiometry in OH700C, a sample crystallizing in a $P4_332$ unit cell, demonstrated that the presence of Mn^{3+} in the spinel structure does not completely preclude Ni/Mn ordering. Generally speaking, this work highlights the importance of careful characterization of "$LiNi_{0.5}Mn_{1.5}O_4$" samples if the goal is to establish composition-structure-properties correlations. Electrode testing confirmed that composition and structure affect the response of the material. However, while worse cycling performance was obtained for the most ordered sample, no difference in the position of the high voltage plateaus was found between samples with different Ni/Mn arrangements. Given the notable entanglement between and crystal-chemical parameters,

more work is needed to completely correlate them to electrochemical properties. However, the detailed picture obtained from this study provides a necessary initial underpinning to the task of achieving control of these parameters through the synthesis conditions. Such control is required to design $LiNi_{0.5}Mn_{1.5}O_4$ electrodes that are closer to the performance limit that the material can offer.

Supplementary Material

Refer to Web version on PubMed Central for supplementary material.

Acknowledgments

The work at LBNL, SUNY Binghamton and SUNY Stony Brook was supported by the Assistant Secretary for Energy Efficiency and Renewable Energy, Office of Vehicle Technologies of the U.S. Department of Energy under Contract No. DE-AC02-05CH11231, as part of the Batteries for Advanced Transportation Technologies (BATT) Program. The program is managed by LBNL for the Department of Energy. Bimghamton and Stony Brook were supported under Subcontracts No. 6807148 and 6517749, respectively. Portions of this research were carried out at the Stanford Synchrotron Radiation Lightsource, a Directorate of SLAC National Accelerator Laboratory and an Office of Science User Facility operated for the U.S. Department of Energy Office of Science by Stanford University. The SSRL Structural Molecular Biology Program is supported by the DOE Office of Biological and Environmental Research, and by the National Institutes of Health, National Center for Research Resources, Biomedical Technology Program (P41RR001209). JC wishes to acknowledge G. Subias (Instituto de Ciencia de Materials de Aragón, Spain) for the collection of the MnO XANES data in this paper, and is indebted to M. Doeff (LBNL, US) for providing access to laboratory facilities. The authors thank the members of the BATT Spinel Focus Group for helpful discussions. CPG also thanks M. Leskes, E. Castillo-Martinez and D. S. Middlemiss (University of Cambridge, UK).

References

1. Wagner FT, Lakshmanan B, Mathias MF. J. Phys. Chem. Lett. 2010; 1:2204–2219.
2. Yang Z, Zhang J, Kintner-Meyer MCW, Lu X, Choi D, Lemmon JP, Liu J. Chem. Rev. 2011; 111:3577–3613. [PubMed: 21375330]
3. Armand M, Tarascon JM. Nature. 2008; 451:652–657. [PubMed: 18256660]
4. Amine K, Tukamoto H, Yasuda H, Fujita Y. J. Electrochem. Soc. 1996; 143:1607–1613.
5. Zhong QM, Bonakdarpour A, Zhang MJ, Gao Y, Dahn JR. J. Electrochem. Soc. 1997; 144:205–213.
6. Goodenough JB, Kim Y. Chem. Mater. 2010; 22:587–603.
7. Xiang HF, Zhang X, Jin QY, Zhang CP, Chen CH, Ge XW. J. Power Sources. 2008; 183:355–360.
8. Wu HM, Belharouak I, Deng H, Abouimrane A, Sun YK, Amine K. J. Electrochem. Soc. 2009; 156:A1047–A1050.
9. Hassoun J, Panero S, Reale P, Scrosati B. Adv. Mater. 2009; 21:4807. -+. [PubMed: 21049499]
10. Talyosef Y, Markovsky B, Lavi R, Salitra G, Aurbach D, Kovacheva D, Gorova M, Zhecheva E, Stoyanova R. J. Electrochem. Soc. 2007; 154:A682–A691.
11. Matsui M, Dokko K, Kanamura K. J. Electrochem. Soc. 2010; 157:A121–A129.
12. Duncan H, Abu-Lebdeh Y, Davidson IJ. J. Electrochem. Soc. 2010; 157:A528–A535.
13. Yang L, Ravdel B, Lucht BL. Electrochem. Solid State Lett. 2010; 13:A95–A97.
14. Cabana J, Zheng H, Shukla AK, Kim C, Battaglia VS, Kunduraci M. J. Electrochem. Soc. 2011; 158:A997–A1004.
15. Arico AS, Bruce P, Scrosati B, Tarascon JM, Van Schalkwijk W. Nat. Mater. 2005; 4:366–377. [PubMed: 15867920]
16. Bruce PG, Scrosati B, Tarascon JM. Angew. Chem.-Int. Ed. 2008; 47:2930–2946.
17. Song HK, Lee KT, Kim MG, Nazar LF, Cho J. Adv. Funct. Mater. 2010; 20:3818–3834.
18. Hull S. Rep. Prog. Phys. 2004; 67:1233–1314.
19. Lee E, Persson KA. Energy Environ. Sci. 2012; 5:6047–6051.

20. Mukerjee S, Yang XQ, Sun X, Lee SJ, McBreen J, Ein-Eli Y. Electrochim. Acta. 2004; 49:3373–3382.
21. Kim JH, Myung ST, Yoon CS, Kang SG, Sun YK. Chem. Mater. 2004; 16:906–914.
22. Kunduraci M, Amatucci GG. J. Electrochem. Soc. 2006; 153:A1345–A1352.
23. Kunduraci M, Amatucci GG. J. Power Sources. 2007; 165:359–367.
24. Pasero D, Reeves N, Pralong V, West AR. J. Electrochem. Soc. 2008; 155:A282–A291.
25. Myung S-T, Komaba S, Kumagai N, Yashiro H, Chung H-T, Cho T-H. Electrochim. Acta. 2002; 47:2543–2549.
26. Reeves N, Kirk CA, West AR. J. Mater. Chem. 2001; 11:249–250.
27. Ma XH, Kang B, Ceder G. J. Electrochem. Soc. 2010; 157:A925–A931.
28. Lazarraga MG, Pascual L, Gadjov H, Kovacheva D, Petrov K, Amarilla JM, Rojas RM, Martin-Luengo MA, Rojo JM. J. Mater. Chem. 2004; 14:1640–1647.
29. Kunduraci M, Al-Sharab JF, Amatucci GG. Chem. Mater. 2006; 18:3585–3592.
30. Fan YK, Wang JM, Ye XB, Zhang JQ. Mater. Chem. Phys. 2007; 103:19–23.
31. Shaju KM, Bruce PG. Dalton Trans. 2008:5471–5475. [PubMed: 19082030]
32. Zhou F, Zhao X, van Bommel A, Xia X, Dahn JR. J. Electrochem. Soc. 2011; 158:A187–A191.
33. Duncan H, Duguay D, Abu-Lebdeh Y, Davidson IJ. J. Electrochem. Soc. 2011; 158:A537–A545.
34. Rodríguez-Carvajal J. Physica B. 1993; 192:55–69.
35. Thompson P, Cox DE, Hastings JB. J. Appl. Cryst. 1987; 20:79–83.
36. Cabana J, Dupré N, Grey CP, Subias G, Caldes MT, Marie AM, Palacín MR. J. Electrochem. Soc. 2005; 152:A2246–A2255.
37. Wang L, Li H, Huang X, Baudrin E. Solid State Ionics. 2011; 193:32–38.
38. Gryffroy D, Vandenberghe RE. J. Phys. Chem. Solids. 1992; 53:777–784.
39. Shannon RD. Acta Cryst. 1976; A32:751–767.
40. Grey CP, Dupré N. Chem. Rev. 2004; 104:4493–4512. [PubMed: 15669160]
41. Lee YJ, Eng C, Grey GP. J. Electrochem. Soc. 2001; 148:A249–A257.
42. Lee YJ, Grey CP. J. Am. Chem. Soc. 1998; 120:12601–12613.
43. Lee YJ, Grey CP. J. Phys. Chem. B. 2002; 106:3576–3582.
44. Carlier D, Menetrier M, Grey CP, Delmas C, Ceder G. Phys. Rev. B. 2003; 67:174103.1–174103 14.
45. Zeng D, Cabana J, Bréger J, Yoon WS, Grey CP. Chem. Mater. 2007; 19:6277–6289.
46. Cabana J, Kang SH, Johnson CS, Thackeray MM, Grey CP. J. Electrochem. Soc. 2009; 156:A730–A736.
47. Ivanova S, Zhecheva E, Stoyanova R, Nihtianova D, Wegner S, Tzvetkova P, Simova S. J. Phys. Chem. C. 2011; 115:25170–25182.
48. Mukai K, Sugiyama J. J. Electrochem. Soc. 2010; 157:A672–A676.
49. Cheetham AK, Hope DAO. Phys. Rev. B. 1983; 27:6964–6967.
50. Goodenough JB, Wickham DG, Croft WJ. J. Phys. Chem. Solids. 1958; 5:107–116.
51. Sugiyama J, Noritake T, Hioki T, Itoh T, Hosomi T, Yamauchi H. Mater. Sci. Eng. B. 2001; 84:224–232.
52. Wills AS, Raju NP, Greedan JE. Chem. Mater. 1999; 11:1510–1518.
53. Kim JH, Yoon CS, Myung ST, Prakash J, Sun YK. Electrochem. Solid State Lett. 2004; 7:A216–A220.
54. Ariyoshi K, Iwakoshi Y, Nakayama N, Ohzuku T. J. Electrochem. Soc. 2004; 151:A296–A303.
55. Wang L, Zhou F, Meng YS, Ceder G. Phys. Rev. B. 2007; 76:165435.
56. Xiao J, Chen X, Sushko PV, Sushko ML, Kovarik L, Feng J, Deng Z, Zheng J, Graff GL, Nie Z, Choi D, Liu J, Zhang JG, Whittingham MS. Adv. Mater. 2012; 24:2109–2116. [PubMed: 22431364]

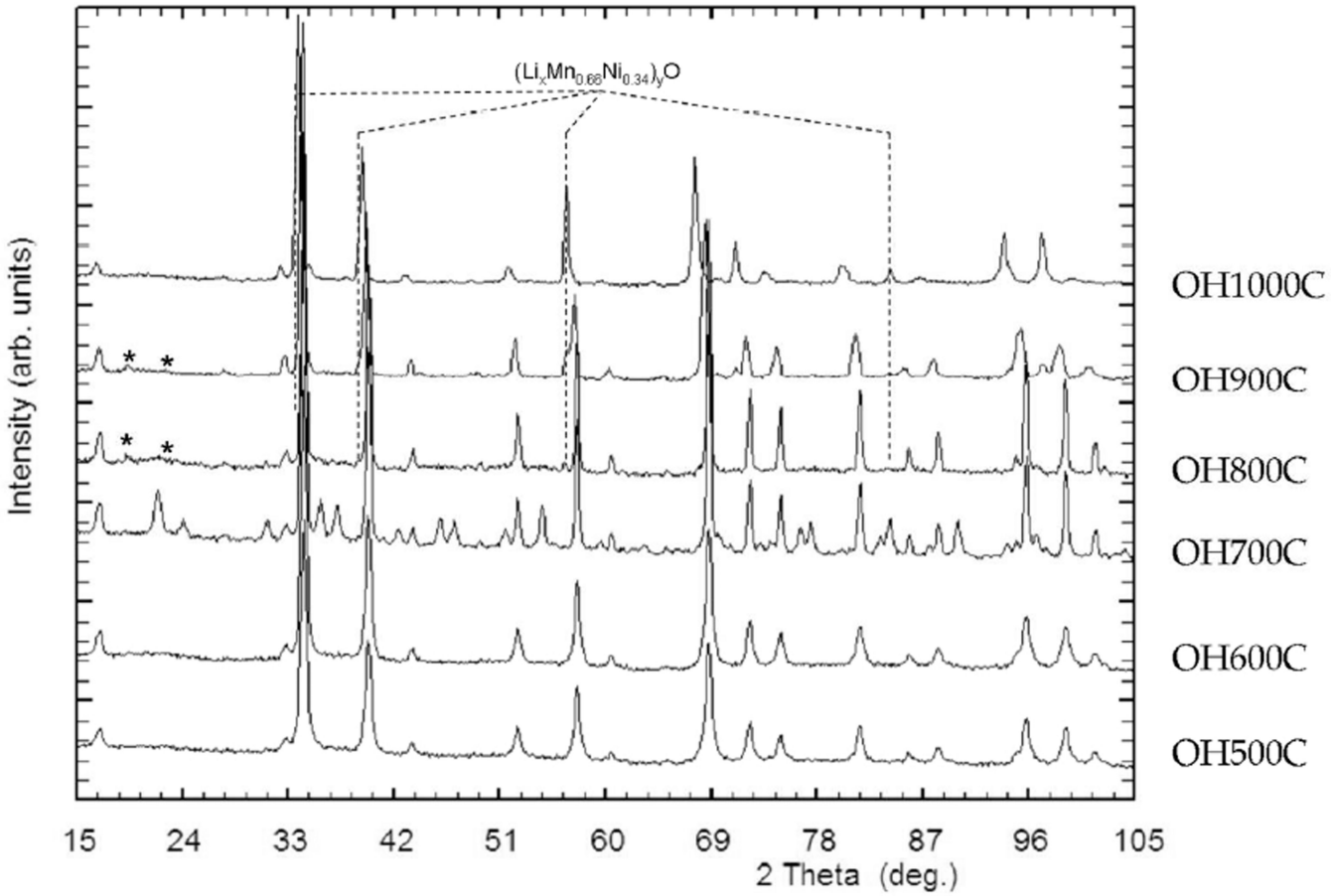

Figure 1.
Neutron powder diffraction pattern of the samples synthesized in this study, as indicated. Resolved reflections of a rocksalt-type secondary phase are indicated by broken lines.

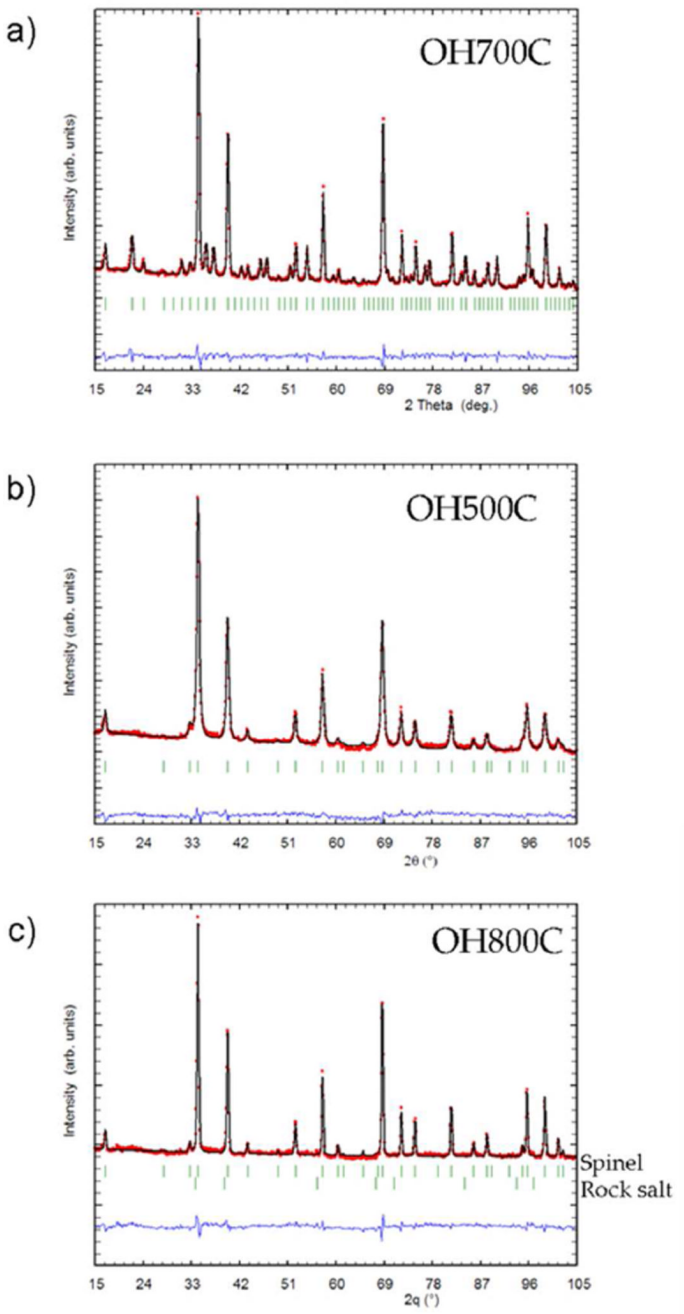

Figure 2.
Neutron powder diffraction pattern (small circles) showing the final Rietveld fit (solid line), with the difference plot below for samples a) OH700C, b) OH500C and c) OH800C.

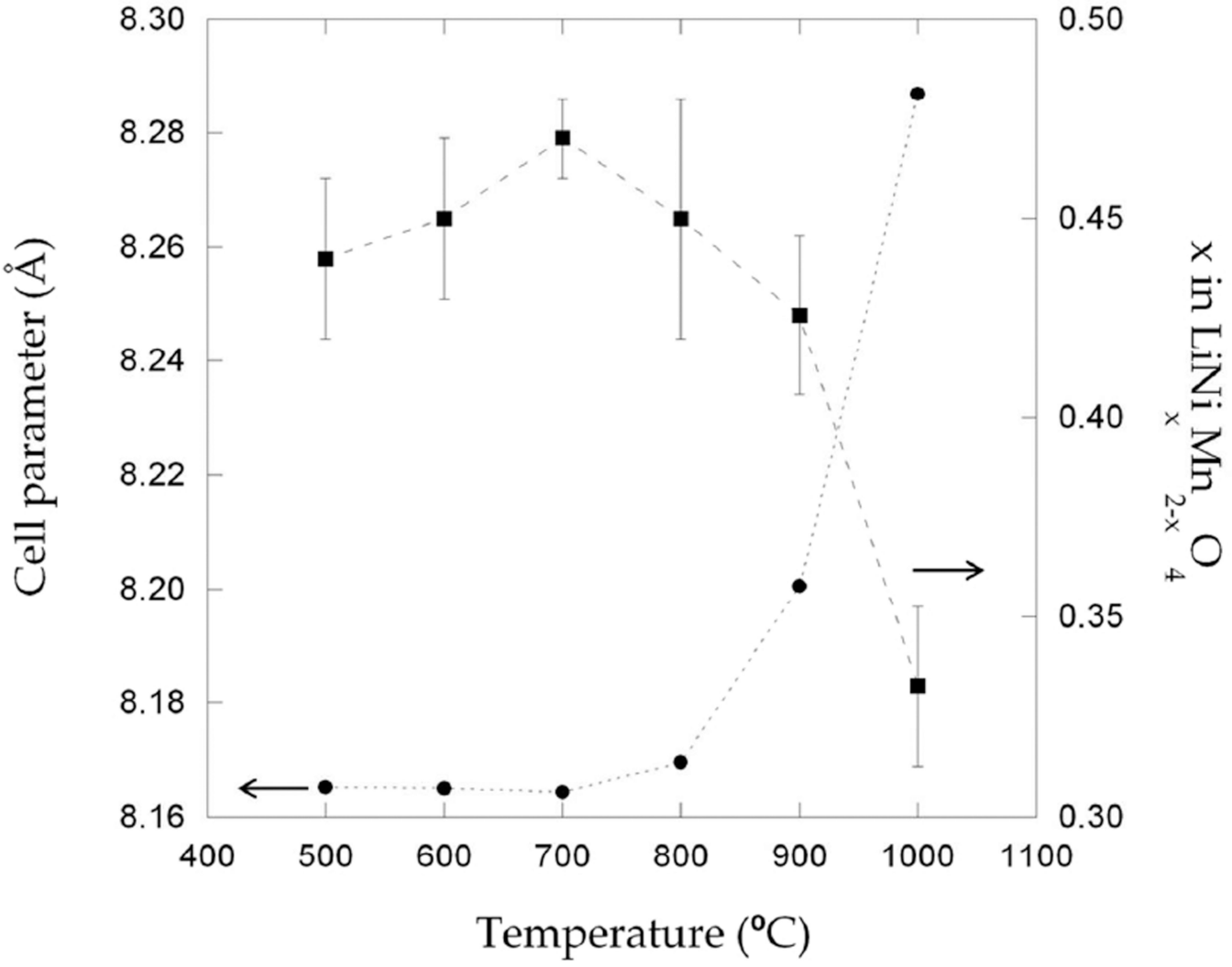

Figure 3.
Variation of the cell parameter and × in $LiNi_xMn_{2-x}O_4$ obtained from Rietveld refinements of neutron diffraction (ND) data with annealing temperature.

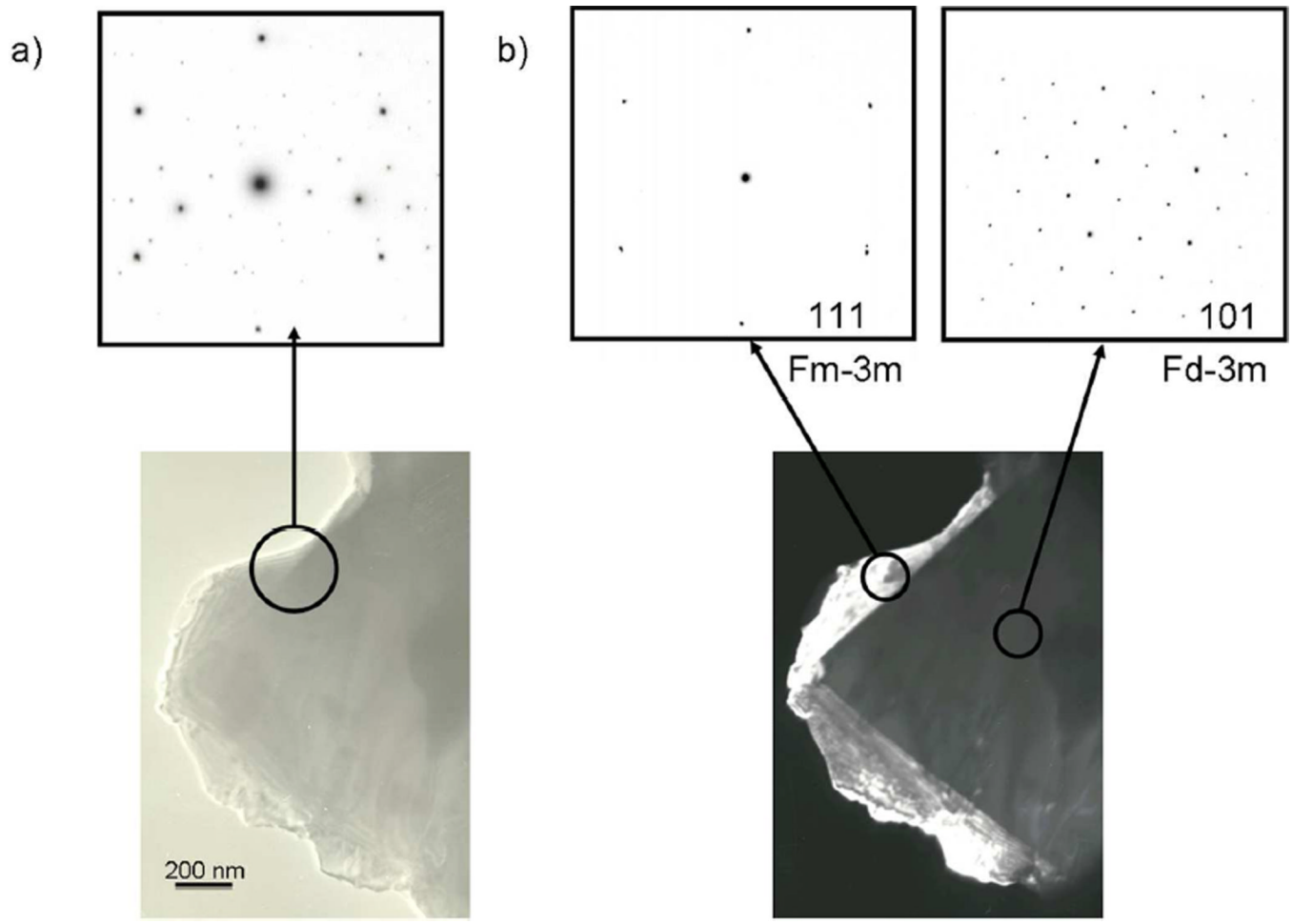

Figure 4.

a) Bright field image of a particle containing different crystallites. The inset shows the corresponding electron diffraction pattern, which results from the overlapping patterns of each crystallite. b) Dark-field image of the particle formed from a (2, -2, 0) reflection that could be indexed to a rock salt-type structure. The insets show the individual zone axis of each crystallite : <111> zone axis for the rock salt phase and <101> zone axis for the spinel phase.

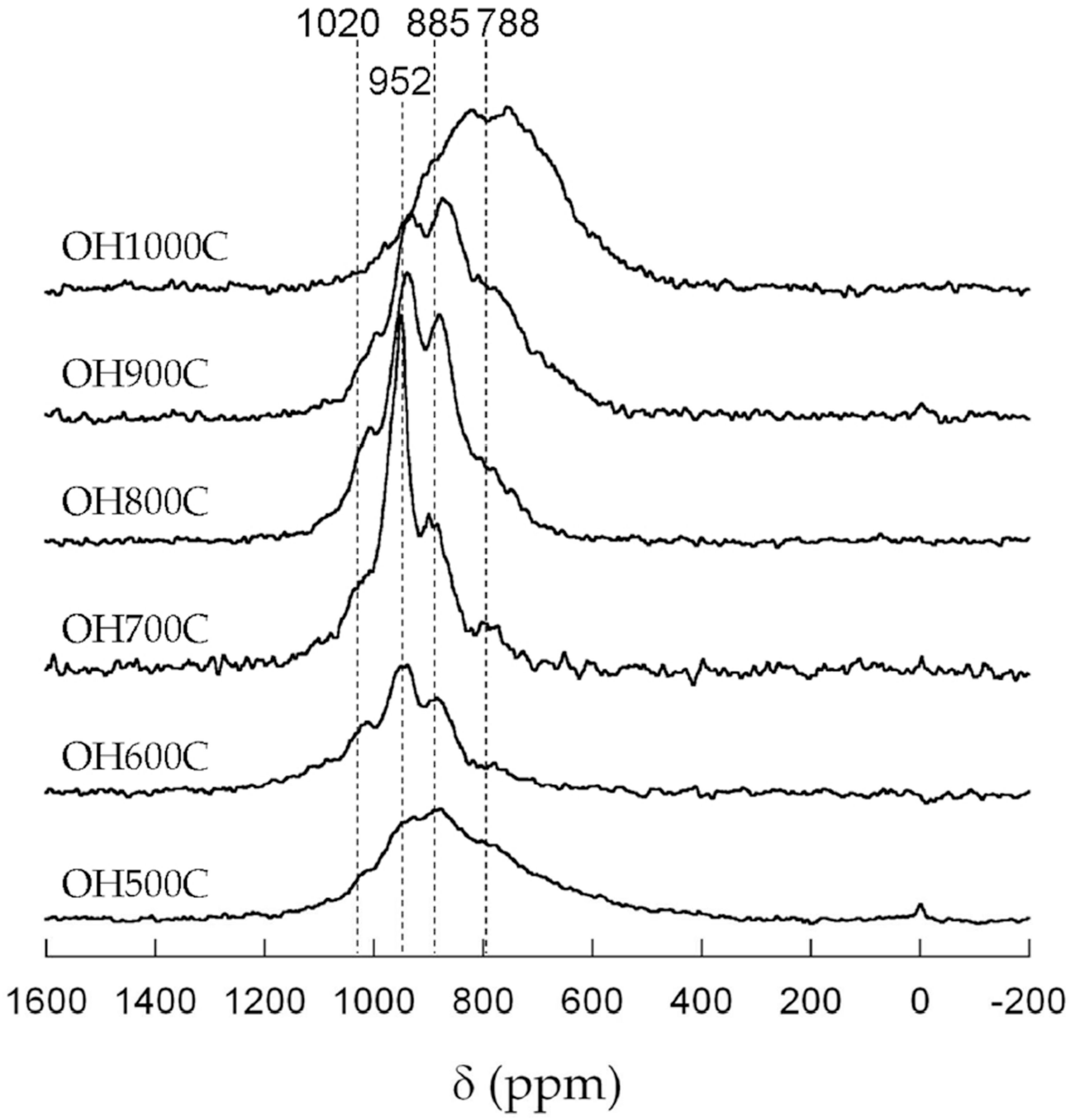

Figure 5.
^{6}Li MAS NMR spectra of the samples synthesized in this study, as indicated. Representative shifts are provided. The existence of minor peaks at 0 ppm in some samples is indicative of the existence of very minor impurities of diamagnetic lithium salts.

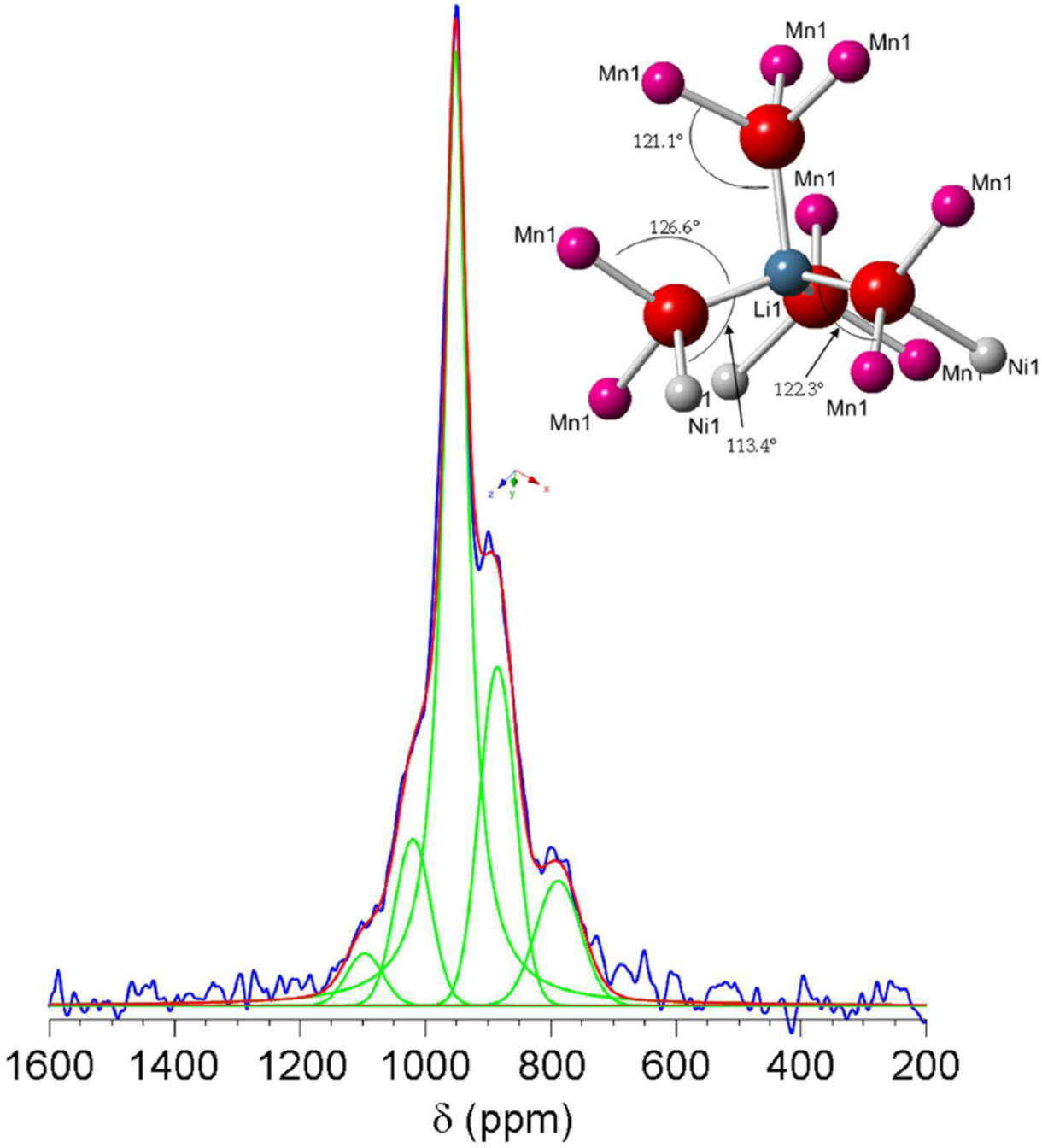

Figure 6.

Deconvolution of the ^{6}Li MAS NMR spectrum of OH700C. See text for details on experimental constraints. The best fit was achieved by using a Lorentzian function for the most intense peak and the largest line broadening for the peak at 788 ppm. Blue: experimental data; red: additive theoretical spectrum; green: deconvoluted peaks. The inset represents the lithium local environment in an ideally ordered spinel structure with formula $LiNi_{0.5}Mn_{1.5}O_4$. Relevant bond angles are provided.

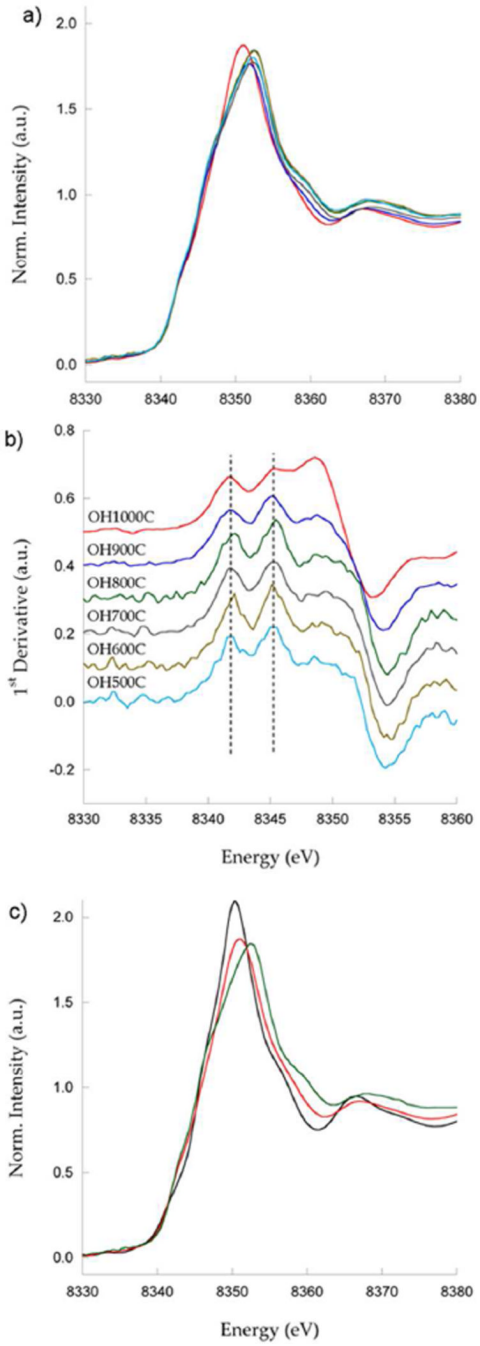

Figure 7.

Ni K edge XANES data for the samples prepared in this study, as indicated. a) experimental spectra, b) first derivative and color code, c) comparison of OH900C and OH1000C with the spectrum of a NiO standard.

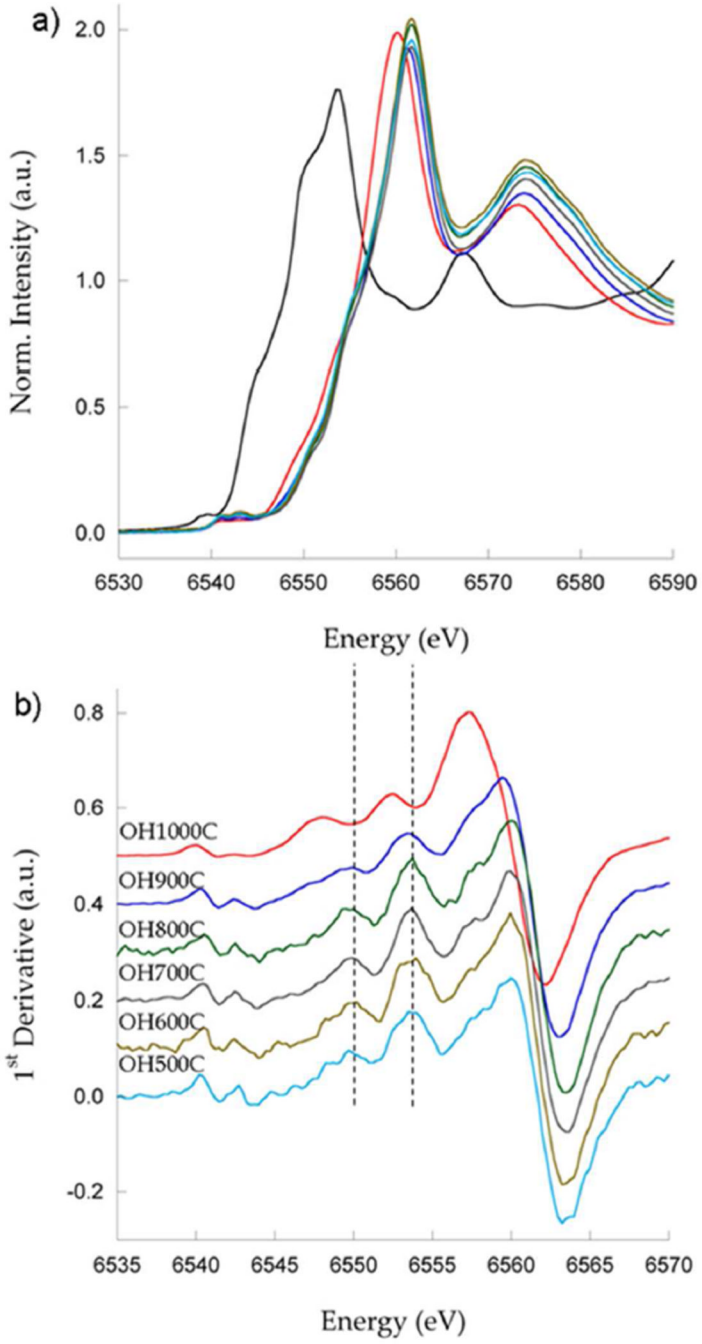

Figure 8.
Mn K edge XANES data for the samples prepared in this study, as indicated. a) experimental spectra with a MnO standard (black), b) first derivative and color code.

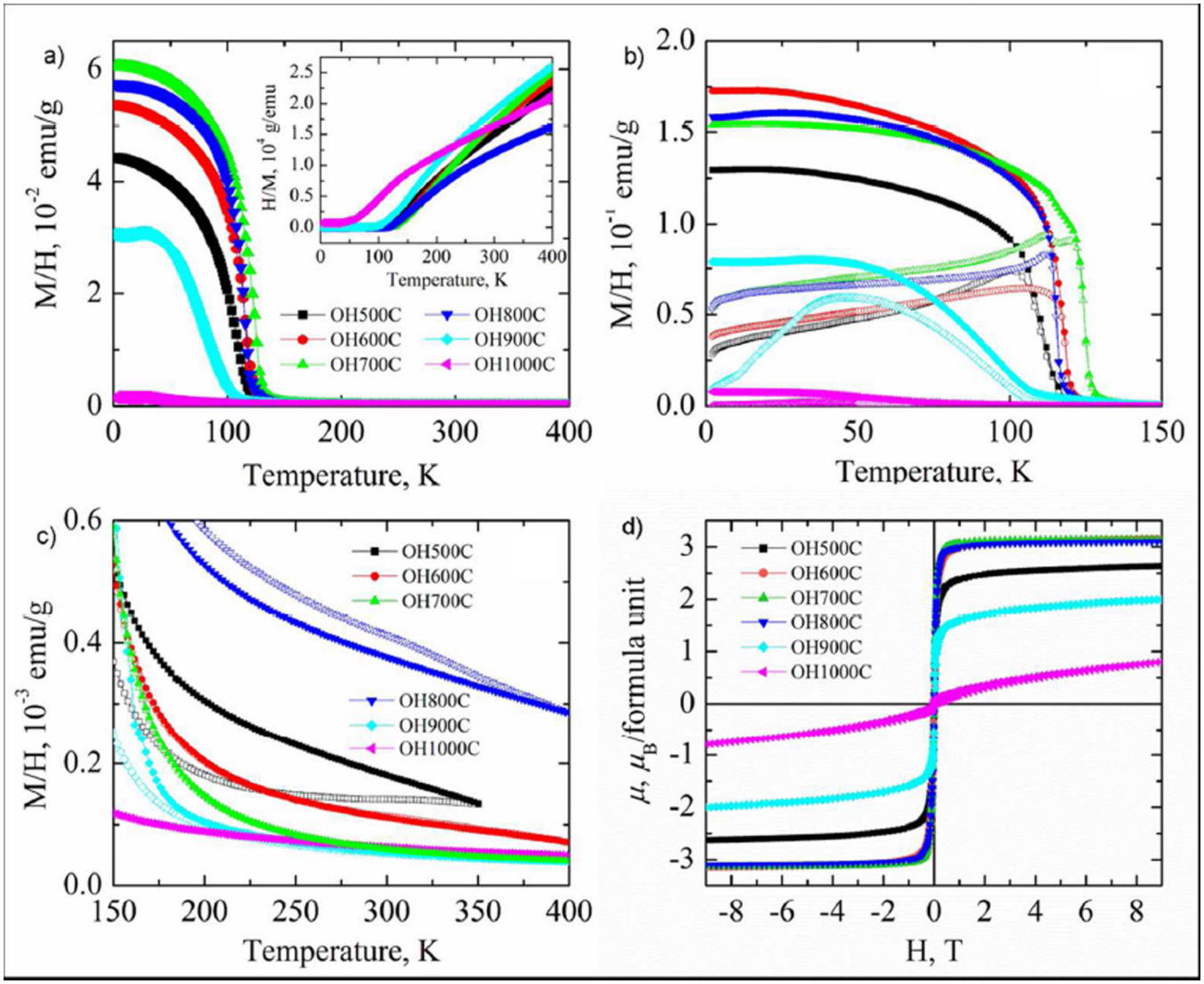

Figure 9.

a) Temperature dependences of the magnetic susceptibility for the samples synthesized in this study, as indicated. The inset shows the reciprocal susceptibility. b) and c) Temperature dependences of field-cooled (solid symbols) and zero-field cooled (open symbols) magnetic susceptibility over the low- and high-temperature region, respectively, for $LiNi_{0.5}Mn_{1.5}O_4$ samples synthesized at various temperatures. d) Magnetization curves at 2 K of $LiNi_{0.5}Mn_{1.5}O_4$ prepared at various temperatures.

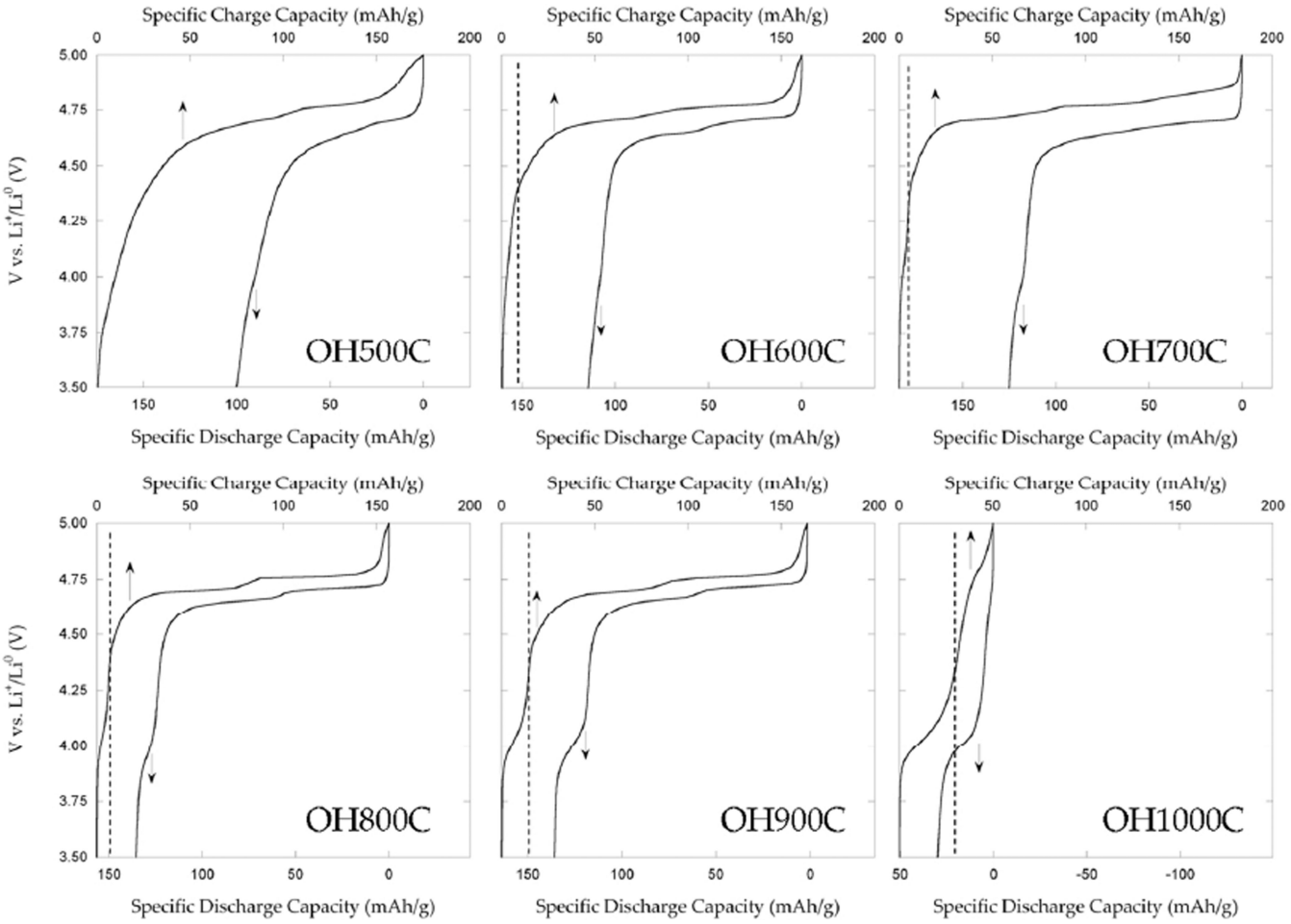

Figure 10.
First cycle of lithium metal half-cells containing the samples synthesized in this study, as indicated, as positive electrodes, cycled at C/10.

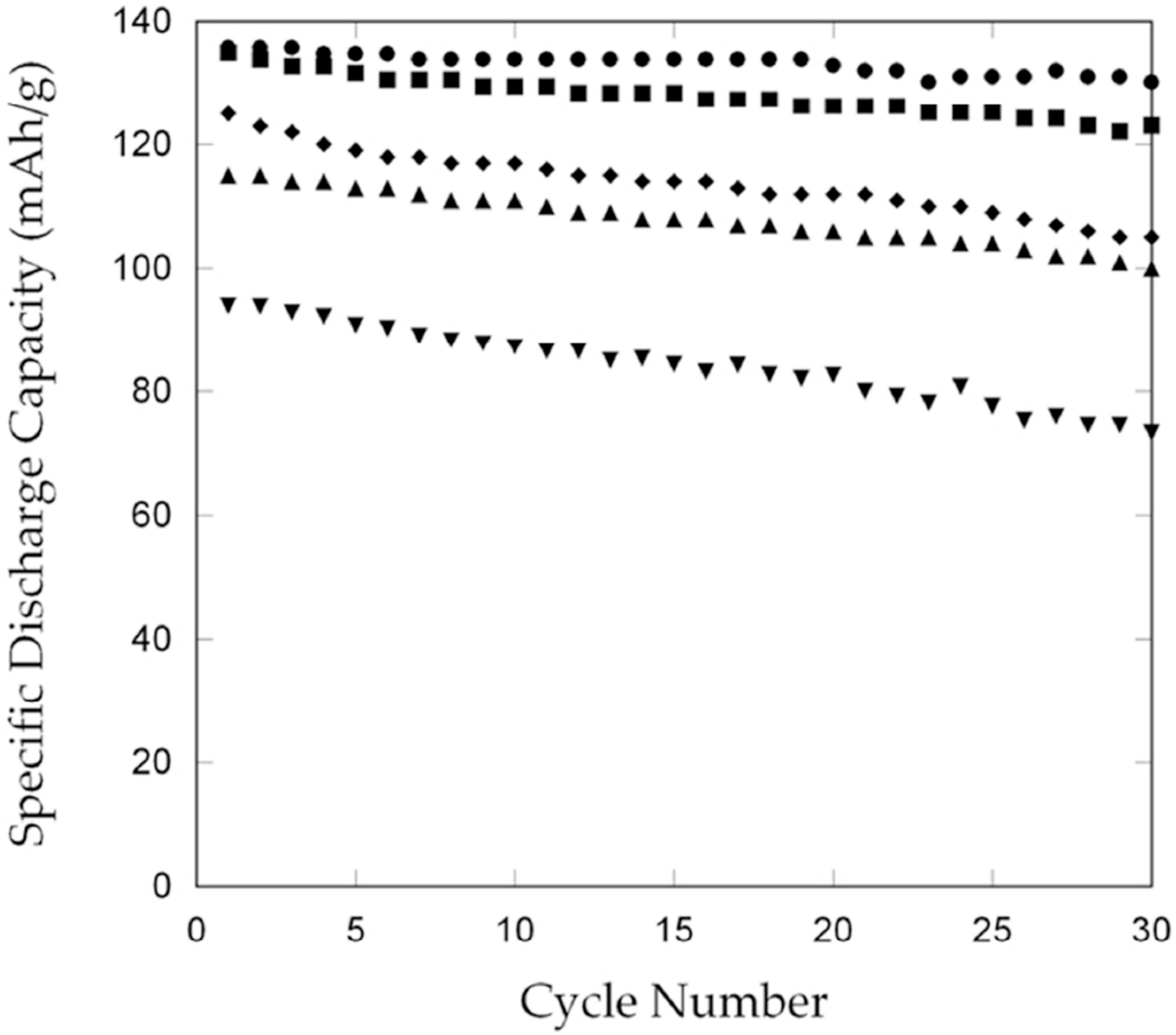

Figure 11.
Specific discharge capacity *vs.* cycle number of lithium cells containing the samples synthesized in this study, as positive electrodes, cycled at C/10. Inverted triangles: OH500C; triangles: OH600C; diamonds: OH700C; squares: OH800C; circles: OH900C.

Table 1

Rietveld refinement results for sample OH700C (space group $P4_332$)

Lattice parameter	a (Å)		8.1644(2)
Fractional coordinates	Mn/Ni x	(*12d*)	0.125
	Mn/Ni y	(*12d*)	0.381(2)
	Mn/Ni z	(*12d*)	0.869(2)
	Ni/Mn x,y,z	(*4b*)	0.625
	Li x,y,z	(*8c*)	0.006(3)
	O1 x,y,z	(*8c*)	0.3866(6)
	O2 x	(*24e*)	0.1471(6)
	O2 y	(*24e*)	0.8584(5)
	O2 z	(*24e*)	0.1258(6)
Occupancies	Mn/Ni	(*12d*)	1.422(8)/0.078(8)
	Ni/Mn	(*4b*)	0.105(5)/0.395(5)
Biso (Å^2)	Mn/Ni (12d)		0.5(2)
	Ni/Mn (4b)		0.6(1)
	Li (8c)		0.8(3)
	O1 (8c)		0.24(9)
	O2 (24e)		0.61(5)
Agreement factors	Rp		15.3
	wRp		13.4
	Rexp		8.86
	$\times^2$		2.28

Table 2

Rietveld refinement results for samples OH500C, OH600C, OH800C, OH900C and OH1000C. The rock salt phase was added in profile matching mode in samples OH800C, OH900C and OH1000C.

Sample			**OH500C**	**OH600C**	**OH800C**	**OH900C**	**OH1000C**
				Spinel phase			
Space group			Fd-3m	Fd-3m	Fd-3m	Fd-3m	Fd-3m
Lattice parameter	a (Å)		8.1652(8)	8.165(1)	8.1696(4)	8.2006(8)	8.287(1)
Fractional coordinates	Mn/Ni x,y,z	(*16d*)	0.5	0.5	0.5	0.5	0.5
	Li x,y,z	(*8a*)	0.125	0.125	0.125	0.125	0.125
	O x,y,z	(*32e*)	0.2632(3)	0.2632(4)	0.2632(3)	0.2632(4)	0.2635(4)
Occupancies	Mn/Ni	(*16d*)	1.56(2)/0.44(2)	1.55(2)/0.45(2)	1.55(3)/0.45(3)	1.57(2)/0.43(2)	1.67(2)/0.333(2)
Biso (Å2)	Mn/Ni	(*16d*)	2(1)	2(1)	2(1)	1(1)	2(1)
	Li	(*8a*)	2(1)	2(1)	1.0(6)	1.6(9)	0.5(7)
	O	(*32e*)	1.1(1)	0.9(2)	0.83(9)	1.0(1)	1.5(1)
				Rocksalt phase			
Space group			-	-	Fm-3m	Fm-3m	Fm-3m
Lattice parameter	a (Å)		-	-	4.152(2)	4.142(1)	4.1473(3)
Agreement factors	Rp		20.7	20.7	30.7	22.1	23.4
	wRp		16.0	16.5	21.4	16.4	17.3
	Rexp		11.76	10.27	15.29	23.21	12.17
	$\times^2$		1.86	2.57	1.95	0.50	2.02

Chem Mater. Author manuscript; available in PMC 2013 August 14.

Table 3

Cation-oxygen bond distances for the samples studied.

Sample	Li-O(Å)	Mn/Ni-O(Å)
OH500C	1.9548(7)	1.9394(7)
OH600C	1.9542(7)	1.9395(7)
OH700C	Li - O1: 2.02(1) Li - O2: 1.93(1) × 3	Mn/Ni (12d) - O1 : 1.911(2) × 2 Mn/Ni (12d) - O1 : 1.909(7) × 2 Mn/Ni (12d) - O2 : 1.907(7) × 2 Ni/Mn (4b) - O2 : 2.047(2) × 6
OH800C	1.9550(7)	1.9409(7)
OH900C	1.9634 (9)	1.9477(9)
OH1000C	1.988(3)	1.9659(1)

Table 4

Results of EDX analysis for samples OH800C, OH900C and OH1000C. For a better accordance to the nominal composition the results of the spinel phase are normalized to 2 and the results of the rock salt phase are normalized to 1. Fractions were calculated using a population of ~30 crystallites for each sample.

Sample	Spinel Mn:Ni ratio	Rock salt Mn:Ni ratio	Crystallite Fraction
OH800C	1.52:0.48	0.66:0.34	89% spinel 11% rock salt
OH900C	1.56:0.44	0.66:0.34	78% spinel 22% rock salt
OH1000C	1.70:0.30	0.63:0.37	70% spinel 30% rock salt

Table 5

Calculation of probabilities for a Li environment with different Ni/Mn ratios in its first cationic coordination shell assuming: i) a completely disordered Fd3m cell with formula $Li[Ni_{0.45}Mn_{1.55}]_{16d}O_4$, ii) a partially ordered $P4_332$ cell with formula $Li[Ni_{0.39}Mn_{0.11}]_{4b}[Mn_{1.42}Ni_{0.08}]_{12d}O_4$, as in OH700C. Comparison with the results of the deconvolution of the ^6Li MAS NMR spectrum of OH700C (Figure 6).

		Fd3m cell	$P4_332$ cell		
Total Ni	**Total Mn**	**Probability**	**Probability**	**^{6}Li shift (ppm)**	**% Intensity**
0	12	0.052	0.006	--	--
1	11	0.172	0.072	788	0.115
2	10	0.266	0.281	885	0.268
3	9	0.250	0.422	952	0.457
4	8	0.159	0.176	1020	0.122
5	7	0.071	0.037	1097	0.038
6	6	0.024	0.001	--	--

Table 6

Summary of critical electrochemical parameters obtained from the cycling of samples in Li metal half cells at C/10. No cycling data is provided for OH1000C due to its poor first cycle performance.

Sample	xLi below 4.4 V	Specific discharge capacity (mAh/g)		% retention
		Cycle 1	Cycle 30	
500C	0.18	94	73	78
600C	0.06	115	100	87
700C	0.07	125	105	84
800C	0.08	135	123	91
900C	0.12	136	130	96
1000C	0.17	29	--	--